Journal of Southeast University (English Edition) Vol. 39, No. 4, pp. 384 - 392 Dec. 2023 ISSN 1003—7985

Comparison analysis of the bearing capacity of rock-socketed piles and sand piles for offshore wind turbines

Zhang Puyang Xiong Lichao Le Conghuan Dong Hongji Ding Hongyan

(State Key Laboratory of Hydraulic Engineering Simulation and Safety, Tianjin University, Tianjin 300072, China)

Abstract: The bearing capacity of rock-socketed piles (RSPs) and sand piles under horizontal loads was compared and analyzed through laboratory-scale model tests. The tests were conducted using phosphogypsum to simulate the underlying rock and compacted sand as the upper layer. Particle analysis tests were conducted prior to the tests to confirm soil uniformity. Cone penetration test (CPT) was performed to evaluate the soil, confirming similar soil conditions for all experimental groups, indicating that any errors arising from soil properties could be neglected. The bearing capacity of RSPs was verified through finite element simulation, the results of which closely matched those of the tests. The results show that the bending moment distribution of RSPs and sand piles is consistent, with their maximum bending moment occurring at a depth of 2-3 times the pile diameter (5 cm). However, the location of the maximum bending moment for RSPs is about 1 pile diameter (5 cm) deeper than that of the sand piles. When the upper layer of sand is shallow, the bearing effect of RSPs is more significant, with an increase in the bearing capacity of about 41% compared to sand piles. In addition, due to the squeezing effect of the rock, the cross-sectional deformation of the RSPs is significantly lower than that of the sand piles.

Key words: offshore wind power; rock-socketed pile (RSP); laboratory test; bearing capacity

DOI: 10.3969/j.issn.1003-7985.2023.04.007

Recently, the demand for renewable energy has increased globally due to growing environmental awareness, making wind power one of the fastest-growing clean energy sources[1-3]. However, traditional offshore sand piles have certain drawbacks in specific marine environments. For example, extreme weather conditions, such as high wind speeds and intense storms, can challenge the foundation's wind resistance[4]. Moreover, in stringent geological conditions, the bearing capacity of sand piles remains limited due to the small friction and cohesion of the soil[5]. In such geological conditions, rock-socketed piles (RSPs) can be a more effective solution due to their increased bearing capacity achieved by embedding the body of the piles in the rock[6]. RSPs have excellent adaptability and load-bearing capacity in marine environments. In addition, they have a longer service life, more reliable long-term stability, and higher economic benefits, which can meet the long-term operation needs of offshore wind farms[7]. By conducting a comparative study of the load characteristics and failure mechanisms of RSPs and sand piles, a safer, more reliable, and more economical foundation system can be proposed for offshore wind power generation. This research is highly significant for the scientific design of RSPs and the growth of the offshore wind power industry.

Numerous scholars have conducted multiple studies on RSPs. Li et al.[8] utilized ABAQUS software to perform three-dimensional finite element analysis on RSPs, revealing that the proportion of frictional resistance to uplift load increases nonlinearly with the rock-socketed depth. Murali et al.[9] analyzed X-ray computed tomography (CT) images at different pile head displacements and discovered three different interface mechanisms: sliding, local shear, and progressive shear. Han et al.[10] performed laboratory tests and found that the failure mode of a rock-socketed monopile under unidirectional horizontal loading is progressive and exhibits two obvious failure zones. Xu et al.[11] deduced the formula for the lateral bearing capacity of RSPs by employing the concept of instantaneous angle of friction.

However, the lack of practical engineering and experimental data on RSPs makes it necessary to conduct an in-depth study on the bearing characteristics of RSPs and compare them with those of sand piles. Herein, we designed and conducted 1∶100 scaled model tests, combining experiments and numerical simulation to investigate the bearing mechanism of RSPs and compare it with that of sand piles. The research results of this paper will provide reliable technical support for the design and construction of offshore wind power plants as well as practical guidance for related research fields.

1 Experimental Materials and Methods

1.1 Experimental model

The laboratory-scale tests described herein were con-

Received 2023-05-20, **Revised** 2023-09-25.

Biography: Zhang Puyang (1978—), male, doctor, associate professor, zpy@tju.edu.cn.

Foundation item: The National Natural Science Foundation of China (No. 52171274).

Citation: Zhang Puyang, Xiong Lichao, Le Conghuan, et al. Comparison analysis of the bearing capacity of rock-socketed piles and sand piles for offshore wind turbines[J]. Journal of Southeast University (English Edition), 2023, 39(4): 384 - 392. DOI: 10.3969/j.issn.1003-7985.2023.04.007.

ducted in a soil tank with dimensions of 0.8 m × 0.8 m × 0.9 m. Two different test conditions were set: pure sandy soil condition and rock-socketing condition, where sand and rock were isotropic without stratification. The offshore wind turbine monopile foundation is a large-diameter steel pipe pile structure, typically 5-8 m in diameter. The pile foundation prototype studied herein had a diameter of $D_p = 5$ m and a wall thickness of $t = 0.01 D_p$ [12]. Owing to the limitations of the laboratory environment, the model was scaled to 1∶100, reducing the length and diameter of the pile. Thus, the diameter of the model pile was set as $D = 5$ cm (see Fig. 1). Model piles are typically composed of materials such as iron, aluminum, or plexiglass, with reduced pile stiffness to account for the reduced stress levels in the model. The value of moment inertia is determined by the wall thickness. Using the same material (steel) as the prototype will result in a small wall thickness and difficulty in controlling the accuracy of the wall thickness. Therefore, plexiglass was used as it has a deformation range within the linear elastic range. The wall thickness of the model pile was calculated to be 5 mm. The material parameters of plexiglass are shown in Table 1.

Fig. 1 Rock-socketed pile model made of phosphogypsum for simulating the rock

Table 1 Material parameters of the pile model used in the test

Material	Density/ ($kg \cdot m^{-3}$)	Young's modulus/GPa	Poisson's ratio	Yield stress/ GPa
Plexiglass	1 180	3	0.32	2.5

As the stiffness of the pile cross-section was reduced, the material used to simulate the rock was also correspondingly replaced. The elastic modulus of the actual rock is typically dozens of GPa, and even small deformation can result in substantial reaction force. To simulate the rock, phosphogypsum was used along with other materials, with proportion shown in Table 2[13]. The produced phosphogypsum had dimensions of 55 cm × 35 cm × 25 cm (see Fig. 1), a density of 2 100 kg/cm^3, an elastic modulus of 1.4 GPa, and a compressive strength of 8.9 MPa[13]. As the stress range in the test was sufficiently small, the boundary effect due to the size of soil tank was negligible.

Table 2 Proportion of phosphogypsum and materials used to simulate the rock %

Phosphogypsum	Phosphorus slag powder	Calcium oxide	Cement	Water reducer	Retarder	Water-cement ratio
85	9	6	5	1	0.3	0.43

The test was conducted on sandy soil collected from the Bohai Sea in Tianjin, China. As low-density sandy soil undergoes continuous compression during loading, its density constantly changes and is difficult to determine. Hence, the sandy soil was compacted using a layer placement method to achieve maximum density during testing. Each layer was 10 cm thick and tamped with weights, and the process was repeated until the required thickness was achieved. However, this tamping process caused a significant disturbance on the surface soil, which can seriously affect its uniformity. To reduce the impact on the surface soil, the soil layer was increased by 5 cm during each 5 cm compaction process, and the excess margin was removed after compaction. After completing each testing condition, the sand was removed, reworked, and then used for the next testing condition. Following the preparation, the soil parameters were measured (see Table 3) and used as the basis for the numerical simulation.

Table 3 Parameters of the sandy soil in the test

Material	Density/ ($kg \cdot m^{-3}$)	Young's modulus/ MPa	Friction angle/(°)	Poisson's ratio	Cohesion yield stress/kPa
Sand	1 689	5.8	41.9	0.3	0

All tests conducted herein were horizontal loading tests; an electric actuator was used as the loading device (see Fig. 2), with a loading displacement of $0.1D$. The electric actuator had a maximum thrust of 1 kN, and the loading speed was controlled to 0.1 mm/s, with a retractable range of 20 cm, which could satisfy the loading deformation requirements. Owing to the size constraints of the electric actuator, it was not possible to load it on the mud surface; therefore, the lowest loading point was moved 2 cm above the mud surface. An iron hoop was installed at the loading point to transfer the load to the pile body through it. The iron hoop ensured a precise height for each loading point. In addition, it ensured that the load was distributed more uniformly at the loading point, avoiding load concentration in the pile. For the purpose of a clear and direct comparison of the experimental results of RSPs and sand piles, we did not consider the influence of externally applied bending moment loads.

Fig. 2 Laboratory-scale test model

Four types of sensors were used in the test (see Fig. 3):

1) Pressure sensor. This sensor was fixed at the tip of the electric actuator and connected by thread, with the other end in contact with the iron hoop at the loading point.

2) Displacement sensor. Positioned on the opposite side of the pile, this sensor measured displacement by monitoring the expansion and contraction of its own pull cord. The end of the pull cord was a magnetic contact attached to the iron hoop in the loading position.

3) Strain gauge. Strain gauges were installed at both sides of the pile at 5-cm intervals (i. e., 1 pile diameter) from the bottom to the top of the outer wall. Before sticking the strain gauge, the measuring point was polished with sandpaper and then cleaned with alcohol. The strain gauges were glued seamlessly to the pile wall, ensuring accurate measurements. A layer of epoxy resin, with an average thickness of < 1 mm, making them resistant to moisture, heat, and compression.

4) Soil pressure sensor. This sensor was installed near the side of the pile, with 5-cm intervals (i. e., 1 pile diameter) in the vertical direction. The reading of the soil pressure sensor was balanced and cleared before loading; thus, we measured the additional value of the soil pressure caused by the pile body deformation rather than the actual soil pressure.

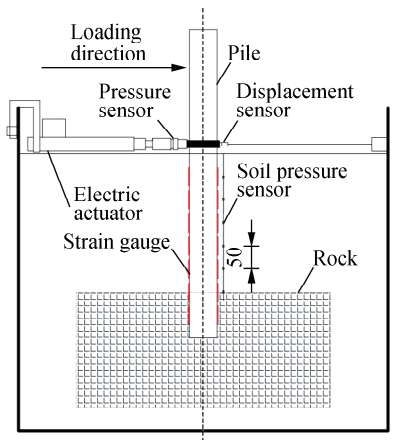

Fig. 3 Deployment of the test model, sensors, and loading device (unit: mm)

Zhang et al.[14] discovered that $2D$ (D represents pile diameter) is the appropriate embedded depth of RSPs under lateral load. Therefore, the embedded depth of the RSP was set at 10 cm. A total of four control tests were performed, and the testing conditions are shown in Table 4.

Table 4 Testing conditions of the four experimental groups

Experimental groups	Conditions	Buried depth/cm	Rock-socketed depth/cm	Measuring depth/cm
1	Sand	35	0	0-35
2	Sand	45	0	0-45
3	Rock	35	10	0-35
4	Rock	45	10	0-45

1.2 Soil assessment

1.2.1 Particle analysis test

In the model test, the structure being studied must be proportionally scaled; however, the soil used in the test cannot be scaled based on the similarity criteria. To prevent the impact of large particles on test results, large particles in the sandy soil were sieved using a 2-mm fine sieve. The particle analysis test mainly determined the soil's gradation and uniformity coefficient; the particle gradation curve of the soil after sieving is shown in Fig. 4.

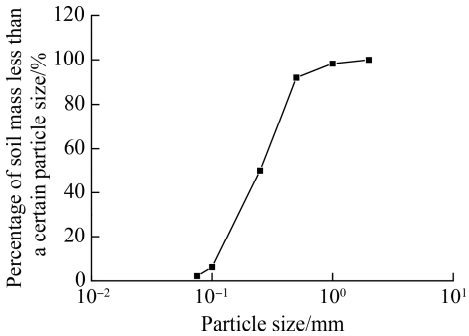

Fig. 4 Grain size distribution of the sandy soil

Fig. 4 shows that the particle size of the sandy soil used in the test was less than 2 mm. The primary components of the soil were fine sand (0.125-0.25 mm) and medium sand (0.25-0.50 mm), accounting for about 80% of the total composition. The uniformity coefficient of the sandy soil was calculated to be $C_u = 3$, and the curvature coefficient was $C_c = 0.96$. Thus, the soil was poorly graded homogeneous soil that met the test requirements.

1.2.2 Cone penetration test

To ensure the consistency of soil compactness throughout the test, the sandy soil in each testing condition was evaluated using the cone penetration test (CPT)[15]. CPT was performed using a cone penetrometer, which comprises a cone tip, tubular pressure sensor, and stainless steel cone-rod (see Fig. 5). The cone tip has a 60°-conical tip with a diameter of 18 mm and a screw hole for connecting the pressure sensor, and it is divided into a conical and cylindrical section. The pressure sensor exhibits an oper-

ating range of 1 kN and a sensitivity of 0.1 N, with screws connecting it to the tip of the cone and cone-rod at both ends. The sensor leads protrude from the upper end of the cone-rod, ensuring that the pressure on the sensor is transmitted solely by the cone tip and not affected by soil contact.

Fig. 5 Cone penetration test for soil assessment in each experimental group

To ensure an accurate measurement in CPT, appropriate measurement points that are not excessively close to the pile body or tank wall must be chosen; points exceedingly close to the pile can disrupt the soil around it, potentially affecting the pile's inclination. Similarly, measurement points extremely close to the tank wall can impact the soil's lateral deformation and increase the lateral friction and resistance of the cone tip. Kim et al. [16] conducted centrifuge CPT tests on different sandy soils and found that a ratio of boundary distance to cone diameter (S/B) greater than seven had no impact on the test results. They also demonstrated that the penetration rate did not affect the cone tip resistance. Therefore, the midpoint position between the pile and tank wall is generally selected to meet testing requirements.

In each group, CPT tests were conducted after loading and unloading, with a maximum thrust of the electric actuator at 600 N and a constant loading rate of 5 mm/s throughout the test. Fig. 6 shows that the end resistance

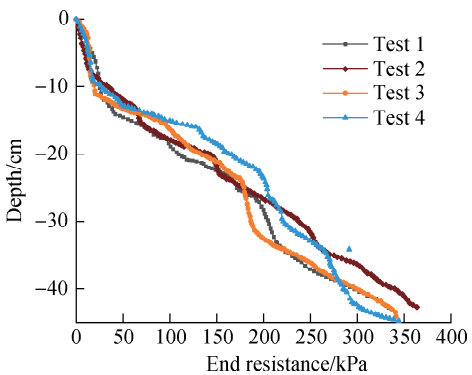

Fig. 6 End resistance-depth curve obtained by the cone penetration test

increases gradually with depth, and the curves for the four tests are highly similar, indicating that the soil conditions for all four tests are consistent.

2 Finite Element Simulation Modeling

The three-dimensional bearing capacity of RSPs simulated by ABAQUS finite element software has been proven reliable[1]. Therefore, herein, we modeled the RSPs using ABAQUS finite element software. As shown in Fig. 7, the numerical simulation model consists of a pile, sand layer, and rock layer. In the finite element tests, the constitutive model of the soil layer is incorporated using the Mohr-Coulomb plasticity model. The contact between the pile and sand was modeled as a frictional contact with a friction coefficient of 0.4, while that between the pile and rock was established as a frictional contact with a friction coefficient of 0.7[17]. In contrast, the constitutive model of the rock layer was simplified into an elasticity model. This simplification is based on the assumption that the mechanical response of the rock remains within the linear elastic range.

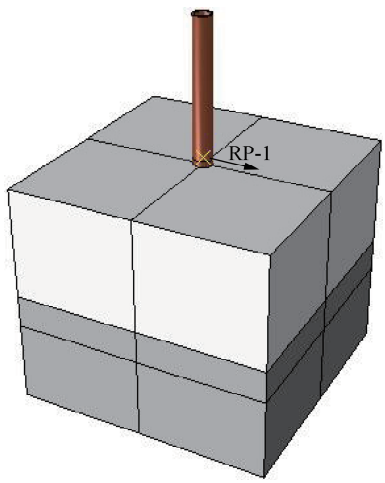

Fig. 7 Numerical simulation model built by ABAQUS

The simulation was performed using static general work steps, with initial and maximum increments of 0.01 and 1, respectively. The minimum increment of the working step was set to 1.0×10^{-5} to avoid lengthy calculations. The loading point was placed at RP-1 and coupled with the pile section in the horizontal plane, and the load-displacement was set to 0.5 cm with a positive x-axis direction. The soil's boundary constraint was fixed at the bottom, with no translation or rotation in any direction, while the soil sides were only limited to horizontal translations and vertical corners. The C3D8R solid unit was used for meshing, with the inner and outer pile grids being as consistent as possible to ensure the calculation's transitivity and accuracy. Finally, the control groups of numerical simulation were set the same as the experimental groups shown in Table 4.

3 Results and Discussion

The data collected during the test included the loading pressure, displacement of the loading point, tensile strain measured by a strain gauge, and soil pressure at various depths.

3.1 Experimental bending moment calculations

Bending moment contrast can be used as an alternative method to pile body deformation contrast, which can eliminate the need for formula fitting and integration and reduce the errors caused by coefficient values. Instead of analyzing pile body deformation, this method involves the comparison of the bending moment at different points along the pile. By using strain gauge data, the cross-sectional bending moment can be calculated at a specific height on the pile, as described by

$$M = \frac{\varepsilon EI}{R} \tag{1}$$

where M is the cross-sectional bending moment at the measuring point; ε is the measured strain value; E is the elastic modulus of the pile; I is the moment of inertia of the cross-section relative to the neutral axis; R is the distance of the measurement point from the center of the section. This approach can provide a more accurate and efficient way of analyzing the behavior of a pile under load.

According to Eq. (1), the bending moment of the piles at various loading displacements was calculated using data obtained from Groups 2 and 4, as shown in Table 4. Since the loading point was 2 cm from the sand surface, the bending moment at the surface layer was not zero. Both graphs in Fig. 8 show that the bending moment first increases, then decreases with the increasing depth, and eventually falls to zero at the pile bottom. As the displacement of the loading point increases, the bending moment at different depths increases to varying degrees, but the overall trend remains the same, with the maximum bending moment at a depth 2-3 times the pile diameter (D = 5 cm). By comparing Figs. 8 (a) and (b), it is evident that the bending moment is larger, and the peak point is deeper under rock conditions. Furthermore, the bending moment decreases sharply in the depth range of 35-45 cm.

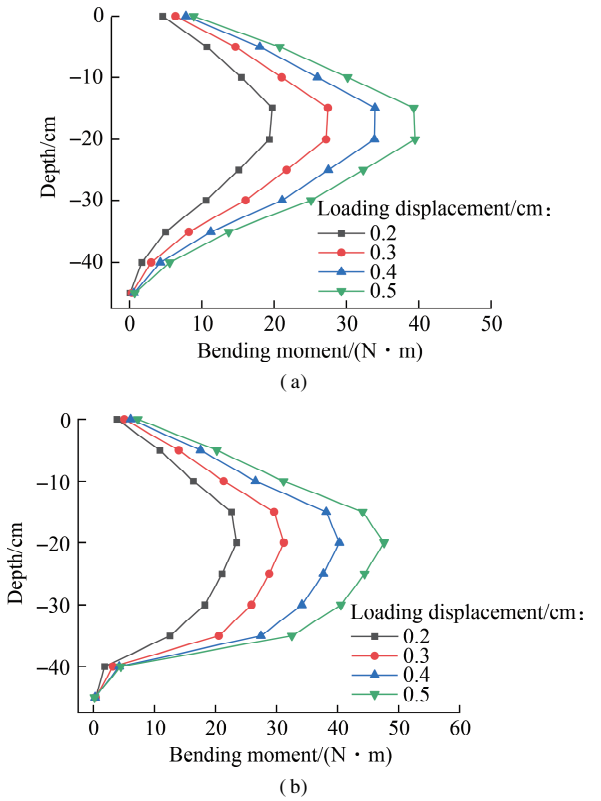

Fig. 8 Distribution of the pile bending moments under a buried depth of 45 cm. (a) Soil condition; (b) Rock condition

3.2 Comparative experimental and simulation studies

3.2.1 Displacement-load curve

In Fig. 9, the results of the finite element analysis and the test are relatively similar and show a consistent trend. By averaging the numerical model and test results, it was found that the pile bearing capacity under rock conditions is improved by about 41% compared to pure sandy soil at a depth of 35 cm and by 35% at a 45 cm depth. This indicates that the rock-socketing effect significantly enhances the bearing capacity and is more significant for shallow overlying soil depth.

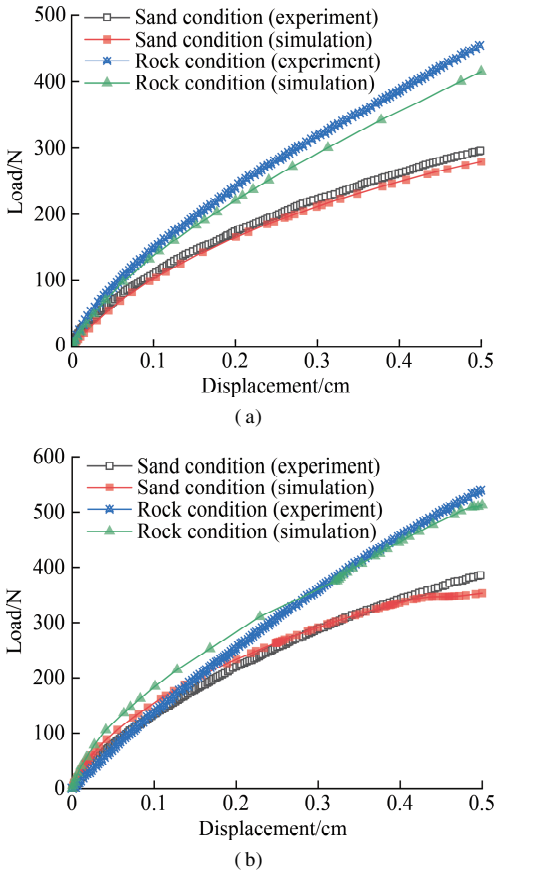

Fig. 9 Experimental and simulation comparison of the displacement-load curve. (a) Depth of 35 cm; (b) Depth of 45 cm

Compared to that at 35 cm, the pile bearing capacity in sandy soil at a depth of 45 cm increased by 25%, while in rock-socketing conditions, it increased by 19%. This implies that increasing the thickness of the overlying soil is beneficial for improving the ultimate bearing capacity of the pile, and the improvement in pure sandy soil condition is more significant than that in rock-socketing condition.

Fig. 10 shows that under an external load, the pile exhibits a rotational tendency. The maximum strain in the soil occurs at the surface, which is at the edge of the rotational plane. In the sand condition, a relatively small strain occurs at the bottom of the pile, and the rotational center is located at one-quarter of the depth from the pile bottom. In the rock condition, almost no strain occurs at the pile bottom, and the rotational center is located at the bottom. This suggests that the rock imposes a constraining influence, limiting the rotational movement and displacement at the pile's base. This trend aligns with the observations made in the study conducted by Zhang et al. [14].

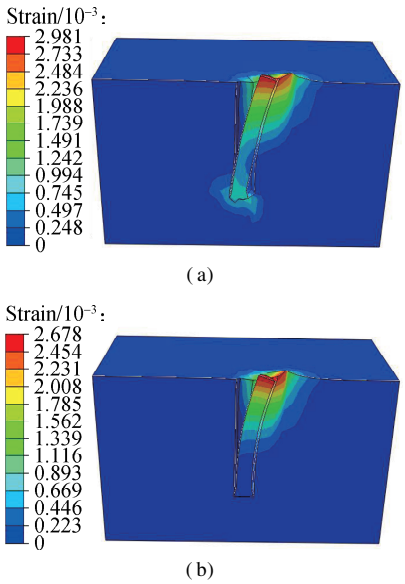

Fig. 10 Simulation comparison of equivalent plastic strain in soil. (a) Sand condition; (b) Rock condition

3.2.2 Bending moment-depth curve

To compare the similarity between the finite element analysis and model test, a numerical comparison is no longer performed. Instead, the moment is normalized by dividing each data set by its peak value, and a simplified comparison is drawn based on curves with a peak value of 1. Two different burial depths when the displacement at the loading point reaches 0.5 cm were compared.

The normalized moment comparison chart (see Fig. 11) shows that the overall trend of the moment is consistent for all different conditions. The bending moment increases downward from the sand surface and then decreases, with the pile bottom bending moment close to 0. The peak bending moment in the sand condition is 15 cm deep, while in the rock condition, it is 20 cm deep. This indicates that the rock-socketing effect has a significant influence on the moment distribution, causing the maximum moment position to shift downward by the distance of 1D.

Fig. 12 shows that the soil stresses within the pile are

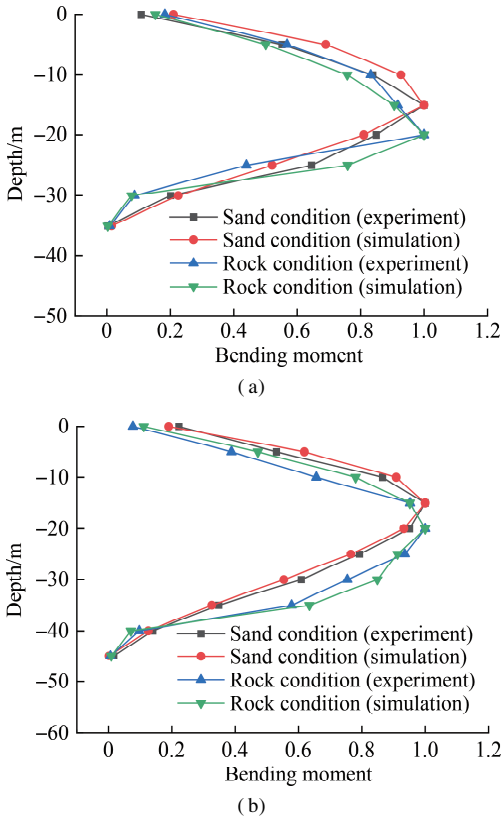

Fig. 11 Comparison of the bending moment-depth curves after experiment and simulation. (a) Depth of 35 cm; (b) Depth of 45 cm

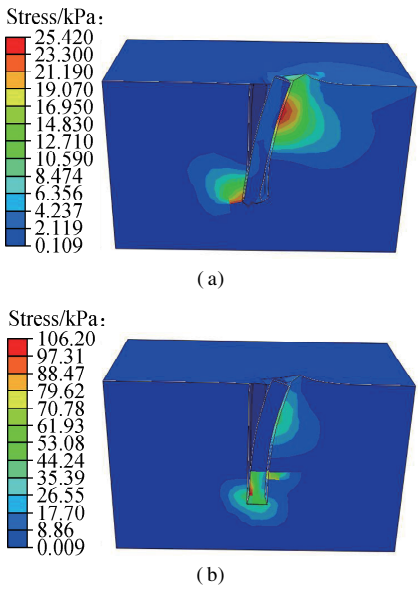

Fig. 12 Simulation comparison of equivalent plastic stress in soil. (a) Sand condition; (b) Rock condition

relatively small. This is primarily because the external load resistance on the pile mainly emerges from the surrounding soil. In the sand condition, the maximum stress is primarily located at the midsection of the pile, with some stress concentration at the pile bottom, mainly on the compressed side of the pile. In the rock condition, as the pile is predominantly influenced by the rock, stress concentrates significantly at the pile bottom, on both the tension and compression sides of the pile, with relatively lower stresses along the pile shaft.

Overall, the maximum stress in the soil is located at the midsection of the pile, gradually decreasing as it spreads outward. This observed pattern validates the accuracy of the bending moment diagram (see Fig. 11). Furthermore, this phenomenon aligns harmoniously with the numerical research findings of Xing et al. [18].

3.3 Simulation analysis of pile cross-section deformation

To analyze the deformation of the pile cross-section, the deformation at a depth of 35 cm (depth of the rock layer surface) in Groups 2 and 4 (see Table 4) is selected (see Figs. 13 and 14). The external load is loaded in the positive direction of the *x*-axis, presented to the right in the graphs. Owing to the extremely small deformation in this case and the insufficient accuracy of experimental measurements, only the finite element method is used for simulation studies.

Under the sand condition, when the cross-section of the pile deformed along the loading direction (*x* direction), the horizontal deformation on the front and back sides of the pile was not equal (see Fig. 13). The maximum horizontal displacement is 0.125 mm, and it is negative because the pile body rotates[19]. The front side of the pile is subject to soil compression, resulting in a smaller deformation, while the back side gradually separates from the soil with the increasing loading displacement, thereby resulting in a larger deformation. Therefore, the cross-section undergoes compression and expansion deformation along the loading direction, and the contour changes from circular to elliptical.

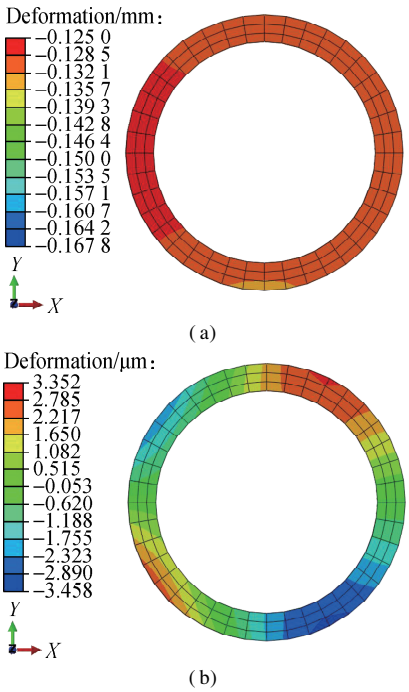

Fig. 13 Sectional deformation of the sand pile at 35-cm depth. (a) Direction *x*; (b) Direction *y*

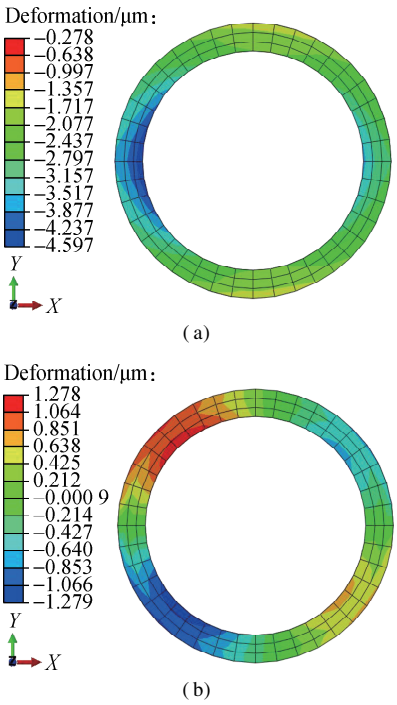

Fig. 14 Sectional deformation of the RSP at 45-cm depth. (a) Direction *x*; (b) Direction *y*

Under the rock condition, the maximum horizontal displacement along the loading direction is three orders of magnitude smaller than that under the sand condition, and the maximum displacement along the *y*-axis is nearly three times smaller (see Fig. 14). The negative displacement values indicate a rotational movement of the pile body. Under the rock condition, the compression deformation of the pile cross-section is significantly reduced, and the tendency for the contour to change from circular to elliptical is not obvious.

This divergence is primarily attributed to the notably higher elastic modulus of rock compared to that of sand. The significant elastic modulus within the rock layer restrains the lateral deformation of the pile body, resulting in a different pile-soil interaction than that in the sand. This can also be interpreted as an outcome of the strong resistance presented by the rock, creating a situation where the pile faces difficulties in undergoing substantial deformation.

4 Conclusions

1) When horizontal load is applied to a pile, the ben-

ding moment along the pile shaft increases from the sand surface to a certain depth and then decreases. The bending moment at the pile tip is almost zero, and the maximum bending moment occurs at a depth 2-3 times the pile diameter (5 cm). For RSPs, the maximum bending moment is greater than that of sand piles, and the depth at which the maximum bending moment occurs is also higher, about 1 pile diameter (5 cm).

2) The bearing capacity of RSPs is about 41% higher than that under pure sandy soil conditions at a depth of 35 cm, while it is about 35% higher at a depth of 45 cm. The improvement effect of rock socketing on pile bearing capacity is more significant, particularly when the overlying soil is shallow.

3) Under pure sandy soil conditions, the bottom section of the pile tends to compress in the loading direction, and the profile changes from circular to elliptical. In rock-socketed conditions, the deformation of the pile section is considerably small due to the squeezing effect of the rock on the pile. This deformation mode results in a different interaction between the pile and rock compared to sandy soil.

References

[1] Le C H, Ren J Y, Wang K, et al. Towing performance of the submerged floating offshore wind turbine under different wave conditions[J]. *Journal of Marine Science and Engineering*, 2021, **9**(6): 633. DOI: 10.3390/jmse9060633.

[2] Zeng X M, Shi W, Feng X Y, et al. Investigation of higher-harmonic wave loads and low-frequency resonance response of floating offshore wind turbine under extreme wave groups[J]. *Marine Structures*, 2023, **89**: 103401. DOI: 10.1016/j.marstruc.2023.103401.

[3] Zhang P Y, Li J Y, Gan Y, et al. Bearing capacity and load transfer of brace topological in offshore wind turbine jacket structure [J]. *Ocean Engineering*, 2020, **199**: 107037. DOI: 10.1016/j.oceaneng.2020.107037.

[4] Zhang P Y, Ding H Y, Le C H, et al. Towing characteristics of large-scale composite bucket foundation for offshore wind turbines [J]. *Journal of Southeast University (English Edition)*, 2013, **29**(3): 300 − 304. DOI: 10.3969/j.issn.1003-7985.2013.03.013.

[5] Xue S, Yue M, Yan Y, et al. Seismic dynamic response analysis of a jacket offshore wind turbine based on an accurate soil-pile model [J]. *Journal of Engineering for Thermal Energy and Power*, 2021, **36**(6): 143 − 151. DOI: 10.16146/j.cnki.rndlgc.2021.06.021. (in Chinese)

[6] Liu X Y, Bai X Y, Zhang M Y, et al. Load-bearing characteristics of large-diameter rock-socketed piles based on ultimate load tests[J]. *Advances in Materials Science and Engineering*, 2020, **2020**: 1 − 12. DOI: 10.1155/2020/6075607.

[7] He R, Ji J, Zhang J S, et al. Dynamic impedances of offshore rock-socketed monopiles[J]. *Journal of Marine Science and Engineering*, 2019, **7**(5): 134. DOI: 10.3390/jmse7050134.

[8] Li G, Zhang J L, Liu J, et al. Study on the uplift bearing capacity of rock-socketed piles[J]. *Soil Mechanics and Foundation Engineering*, 2021, **58**(3): 203 − 208. DOI: 10.1007/s11204-021-09729-9.

[9] Murali A K, Tran K M, Haque A, et al. Experimental and numerical investigation of the load-bearing mechanisms of piles socketed in soft rocks[J]. *Rock Mechanics and Rock Engineering*, 2022, **55**(9): 5555 − 5576. DOI: 10.1007/s00603-022-02954-0.

[10] Han B, Wang B G, Dai S, et al. Bearing failure mechanism of rock-socketed monopile foundation for offshore wind turbine in weathered-granite seabed[J]. *Marine Georesources and Geotechnology*, 2023, **41**(9): 1026 − 1037. DOI: 10.1080/1064119x.2022.2116370.

[11] Xu F, Dai G L, Gong W M, et al. Lateral loading of a rock-socketed pile using the strain wedge model based on Hoek-Brown criterion [J]. *Applied Sciences*, 2022, **12**(7): 3495. DOI: 10.3390/app12073495.

[12] Det Norske Veritaa. Design of offshore wind turbine structures: DNV-OS-J101[P]. 2014.

[13] Liang F F, Zhang H G, Luo Y, et al. Preliminary experimental research on the elastic modulus and Poisson's ratio of cast-in-place phosphogypsum[J]. *Journal of Guizhou University (Natural Sciences)*, 2013, **30**(2): 81 − 85. DOI: 10.15958/j.cnki.gdxbzrb.2013.02.014. (in Chinese)

[14] Zhang P Y, Dong H J, Le C H, et al. Finite element analysis of the horizontal load-bearing characteristics of offshore wind turbine rock-socketed piles[J]. *Journal of Harbin Engineering University*, 2021, **42**(1): 132 − 138. DOI: 10.11990eu.20195066. (in Chinese)

[15] Tong L Y, Wang Q, Du G Y, et al. Determination of undrained shear strength using piezocone penetration test in clayey soil for bridge foundation[J]. *Journal of Southeast University (English Edition)*, 2011, **27**(2): 201 − 205. DOI: 10.3969/j.issn.1003-7985.2011.02.018.

[16] Kim J H, Choo Y W, Kim D J, et al. Miniature cone tip resistance on sand in a centrifuge[J]. *Journal of Geotechnical and Geoenvironmental Engineering*, 2016, **142**(3): 1 − 13. DOI: 10.1061/(asce)gt.1943-5606.0001425.

[17] Gutiérrez-Ch J G, Senent S, Melentijevic S, et al. A DEM-based factor to design rock-socketed piles considering socket roughness[J]. *Rock Mechanics and Rock Engineering*, 2021, **54**(7): 3409 − 3421. DOI: 10.1007/s00603-020-02347-1.

[18] Xing X B, Li X Y, Li W, et al. Numerical analysis of the end-suspended pile and the rock-socketed pile bearing capacity of a soil-rock composite foundation pit[J]. *Advances in Civil Engineering*, 2022, **2022**: 1 − 15. DOI: 10.1155/2022/1199548.

[19] Li Y F, Zhao J H, Xiong Y, et al. Experimental and theoretical research on large-diameter rock-socketed pile embedded depth[J]. *Archives of Civil Engineering*, 2021, **67**(2): 537 − 550. DOI: 10.24425/ace.2021.137184.

海上风电机组嵌岩桩与砂土桩承载力对比分析

张浦阳　熊粒超　乐丛欢　董宏季　丁红岩

（天津大学水利工程与安全国家重点实验室，天津 300072）

摘要：通过室内缩尺模型试验，比较和分析了嵌岩桩（RSP）和砂土桩在水平荷载下的承载能力. 试验使用磷石膏来模拟底部岩石，采用夯实法制作上层砂土. 试验前进行了颗粒分析试验以确认土壤的均匀程度. 采用圆锥负荷试验（CPT）评估土壤，确认所有试验分组的土壤条件相似，即土体性质引起的误差可以忽略不计. 通过有限元模拟对嵌岩桩的承载能力进行了验证，数值模拟结果与试验结果吻合良好. 研究表明：嵌岩桩和砂土桩的弯矩分布一致，桩身最大弯矩的位置在 2 ~ 3 倍桩径深度处，但嵌岩桩的最大弯矩位置比砂土桩深约 1 倍桩径（5 cm）；当上层覆土较浅时，嵌岩桩的承载效果更显著，承载力相对于砂土桩增加约 41%；由于岩石的挤压效应，嵌岩桩的横截面变形明显小于砂土桩.

关键词：海上风电；嵌岩桩；室内试验；承载力

中图分类号：TU473　文献标识码：A